arXiv:1911.01375v1 [physics.atom-ph] 4 Nov 2019

Highly nonlinear ionization of atoms induced by intense high-harmonic pulses

Björn Senfftleben,[1] Martin Kretschmar,[1] Andreas Hoffmann,[1] Mario Sauppe,[1,2] Johannes Tümmler,[1] Ingo Will,[1] Tamás Nagy,[1] Marc J. J. Vrakking,[1] Daniela Rupp,[1,2,*] and Bernd Schütte[1,†]

[1] *Max-Born-Institut, Max-Born-Strasse 2A, 12489 Berlin, Germany*

[2] *Current address: ETH Zurich, John-von-Neumann-Weg 9, 8093 Zürich, Switzerland*

Intense extreme-ultraviolet (XUV) pulses enable the investigation of XUV-induced nonlinear processes and are a prerequisite for the development of attosecond pump - attosecond probe experiments. While highly nonlinear processes in the XUV range have been studied at free-electron lasers (FELs), high-harmonic generation (HHG) has allowed the investigation of low-order nonlinear processes. Here we suggest a concept to optimize the HHG intensity, which surprisingly requires a scaling of the experimental parameters that differs substantially from optimizing the HHG pulse energy. As a result, we are able to study highly nonlinear processes in the XUV range using a driving laser with a modest ($\approx$ 10 mJ) pulse energy. We demonstrate our approach by ionizing Ar atoms up to Ar^{5+}, requiring the absorption of at least 10 XUV photons.

Three key features of intense XUV pulses from FEL and HHG sources have opened up new possibilities for a range of fields from life science to material science and fundamental physics: (i) Intense XUV pulses provide the possibility to perform pump-probe experiments, in which a first XUV pump pulse initiates dynamics in an atom or a molecule, and these dynamics are probed by a second, time-delayed XUV probe pulse. This capability has been extensively used with femtosecond time resolution at FELs (see e.g. Ref. [1]) and has been implemented with attosecond time resolution using HHG sources [2, 3]. (ii) Intense, coherent XUV pulses have enabled single-shot coherent diffractive imaging (CDI) of isolated nanotargets with a resolution in the tens of nanometers range. While these experiments are predominantly performed at FELs [4], CDI on He nanodroplets using an intense HHG source was recently reported [5]. (iii) High XUV intensities enable the study of nonlinear optics in this spectral range. Examples include multiple ionization of atoms [6] and XUV-driven four-wave mixing schemes [7].

Advantages of HHG sources compared to FELs include their smaller size and lower costs resulting in easier access to these sources. Another important point is that two-color XUV-optical pump-probe experiments, which are one of the preferred applications of ultrashort XUV pulses, are challenging at FELs due to timing jitter between the optical and XUV beams [8]. Such experiments are routinely performed using HHG sources, with a time resolution extending into the attosecond domain, given the fact that attosecond pulses based on HHG have been generated for more than 10 years [9].

The most common scheme used to generate intense HHG pulses requires powerful near-infrared (NIR) pulses that are loosely focused into a gas medium to increase the generation volume [3, 10–13]. It has been shown that the HHG pulse energy increases with increasing NIR focal length [14]. In contrast, we demonstrate in this paper that for a given laboratory size the XUV intensity on target can be optimized by using an NIR focusing element with a relatively short focal length. This enables the generation of a smaller XUV beam waist radius in the experiment and a higher XUV beamline transmission. As a result, we achieve an XUV intensity of 7×10^{14} W/cm^2, allowing us to study highly nonlinear processes, which we demonstrate in this paper by ionizing neutral Ar atoms up to Ar^{5+}.

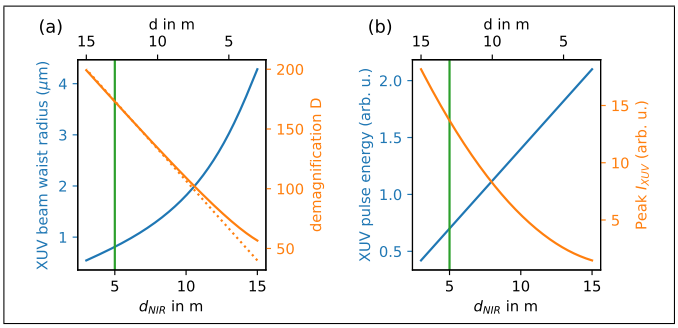

FIG. 1: Calculated scaling of the XUV parameters as a function of the NIR focal length, assuming a total HHG beamline length of 18 m and an XUV focusing mirror with a focal length of 75 mm (corresponding to the conditions in our laboratory). (a) XUV beam waist radius (blue curve) and demagnification resulting from simulations using Gaussian beams (solid orange curve) and calculated according to $D \approx d/f_{XUV}$ (dotted orange curve), where d is the distance from the HHG source to the XUV mirror. (b) Anticipated XUV pulse energy (blue curve) and XUV peak intensity on target (orange curve). The green line corresponds to the position of the NIR focal plane in our setup.

Investigations on HHG scaling have shown that the HHG conversion efficiency may be preserved when varying the laser power, as long as all relevant parameters such as the focusing geometry and the gas pressure and length of the HHG medium are scaled appropriately [15]. One can further assume that the NIR intensity used to optimize the HHG conversion efficiency is nearly independent of the chosen experimental conditions, given that

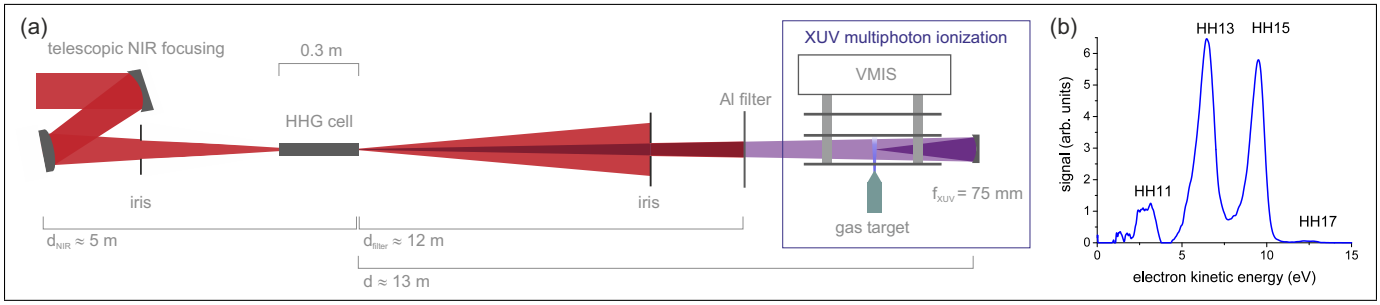

FIG. 2: (a) Experimental setup, see text for details. (b) Photoelectron spectrum of Ar produced by the XUV pulses in the VMIS, showing contributions due to the ionization of high harmonics (HH) with orders between 11 and 17.

the NIR intensity is dictated by phase-matching conditions that are largely determined by the choice of laser wavelength and target gas. As a result, the XUV intensity obtained directly behind the generation medium is to a good approximation independent of the NIR focusing geometry. Therefore, in order to optimize the peak XUV intensity in the experiment, we apply the following strategy: (1) We choose a beamline geometry leading to a large demagnification $D = w_{XUV,source}/w_{XUV,focus}$ (where $w_{XUV,source}$ is the XUV beam waist radius at the HHG source and $w_{XUV,focus}$ is the XUV beam waist radius after focusing). (2) The HHG beamline transmission is optimized by using as few XUV optical elements (filters, mirrors) as possible, as each of these elements introduces high losses.

To study how the demagnification of the XUV beam radius depends on the distance between the NIR focusing element and the focal plane d_{NIR}, we have performed calculations based on Gaussian beams in the paraxial approximation. In these calculations, we have assumed that our laboratory allows a maximum distance of 18 m between the last NIR mirror preceding the HHG source and the mirror that focuses the XUV radiation onto the target. Furthermore, an XUV mirror with a focal length of $f_{XUV} = 75$ mm was assumed, which is the shortest focal length that can be used in combination with our velocity-map imaging spectrometer (VMIS). The results of the calculations are shown in Fig. 1. The XUV beam waist radius in the experiment (blue curve in Fig. 1(a)) increases rapidly with increasing d_{NIR}, both due to the increasing XUV source size (as a result of the increasing NIR focus) and the decreasing demagnification. The demagnification calculated by Gaussian optics (solid orange curve) is in good approximation equal to $D \approx d/f_{XUV}$ for short focal lengths (dotted orange curve), where d is the distance from the HHG source to the XUV mirror. The two curves deviate for long NIR focal lengths where the XUV beam has a very low divergence. In the limit of a collimated XUV beam, the demagnification would increase with d_{NIR} because of the increasing XUV source size. In our experimental setup, we chose $d \approx 13$ m. This results in a demagnification of 173, independent of whether we assume Gaussian optics or demagnification according to simple geometrical optics.

The global HHG scaling laws presented in Ref. [15] show that a constant HHG conversion efficiency can be obtained following the change of one parameter (e.g. the NIR pulse energy), if all other relevant parameters (including the NIR focal length and the NIR beam size before focusing) are changed accordingly. In particular, the NIR intensity needs to be kept constant both before focusing (to avoid damage of the focusing optics) and at the focus (for optimal phase matching). This results in an expected linear increase of the XUV pulse energy as a function of the NIR focal length [15], as shown in Fig. 1(b) (blue curve). The expected XUV intensity (orange curve) shows a contrary behavior: It increases with decreasing f_{NIR}, since the smaller XUV focal spot size more than compensates for the lower XUV energy that is obtained.

According to these scaling laws, the use of a very short NIR focal length would be most advantageous. However, under such conditions the divergence of the XUV beam is substantial, and restrictions due to finite XUV filter and mirror apertures (which cannot be made arbitrarily large) have to be taken into account. Therefore, we have performed first experiments using $d \approx 13$m. Besides offering a large demagnification, a further advantage of this beamline geometry is the occurrence of a comparably low NIR intensity on the Al filter that is used to block the NIR light co-propagating with the XUV beam. This removes the need for additional Si / SiC [16] or antireflective coated mirrors [17], which are often used in high-power HHG applications to attenuate the NIR intensity.

Our experimental setup is shown in Fig. 2(a). An optical parametric chirped pulse amplification (OPCPA) system that was developed in-house is used to drive HHG. This system consists of a three-stage optical parametric amplifier, pumped by a home-built frequency-doubled Yb:YAG thin disk laser that operates at 100 Hz repetition rate. Ultrashort seed pulses from a commercial Yb:KGW front-end are amplified to pulses with an energy of up to 30 mJ and a duration of 8 fs in a spectral

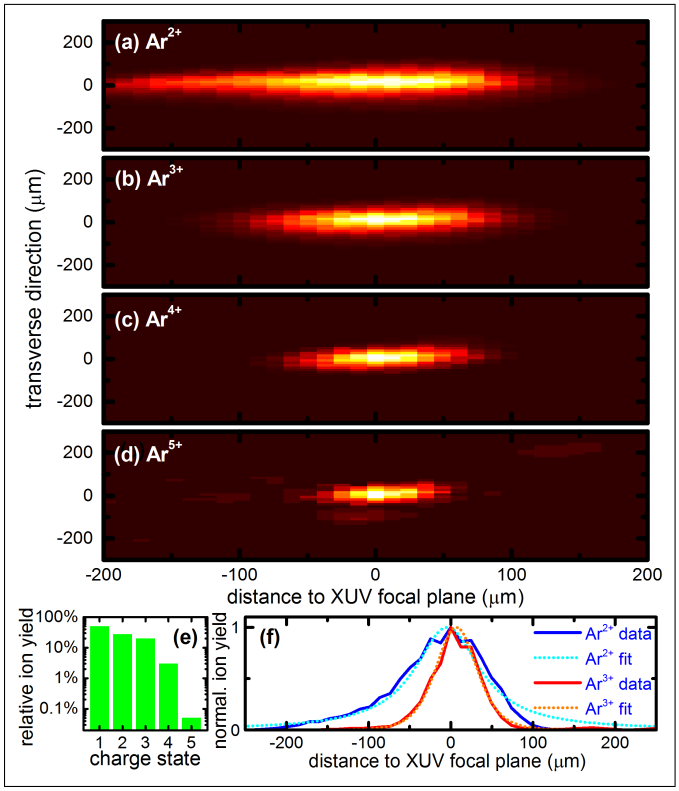

FIG. 3: Spatial distributions of (a) Ar^{2+}, (b) Ar^{3+}, (c) Ar^{4+} and (d) Ar^{5+} ions, where the horizontal axis refers to the XUV propagation axis and the vertical axis refers to the transverse direction. Each ion distribution was normalized to its maximal value. Note that the extension in the transverse direction is limited by the spatial resolution of about 60 μm. Note further that some noise is visible in (d) due to the low signal level. (e) Relative ion contributions at the XUV focal plane. (f) The solid curves represent transversely integrated normalized Ar^{2+} and Ar^{3+} ion distributions. In these measurements a second Al filter was inserted to avoid saturation of the individual ion yields. The dotted curves are fits to the ion distributions to extract the Rayleigh lengths, see text for details.

window from 700 nm to 1025 nm [18]. A telescope consisting of a concave ($f = 1.5$ m) and a convex mirror ($f = -1$ m) is used to focus the NIR pulses. This configuration has the advantages that astigmatism can be compensated and that the distance of the focal plane from the last curved mirror can be easily adjusted. In our setup the f-number of the NIR beam is ≈ 400, and the distance between the last NIR mirror and the NIR focal plane is about 5 m. A motorized iris is placed behind the last NIR mirror to optimize the HHG yield, and we measured an NIR driving energy of 11 mJ behind this iris (for an aperture of 10 mm). A 30 cm long gas cell is placed 10 cm in front of the focus, and is statically filled with Xe using a backing pressure of 7 mbar. We have performed gas dynamics simulations that indicate a reduced pressure of 1.1 mbar to be present within the cell. A 100 nm thick Al filter is placed 12 m downstream from the HHG cell and is used to block the co-propagating NIR light. The XUV pulses are focused into the interaction zone of the VMIS using a spherical B_4C coated mirror with a focal length of 75 mm. Ar atoms are injected into the instrument using a piezoelectric valve. The central part of the atomic beam is selected by a molecular beam skimmer with an orifice diameter of 0.5 mm. Ion distributions are recorded in a spatially-resolved manner along the XUV propagation axis using the spatial imaging mode of the VMIS [19]. In addition, the HHG beam diameter can be measured by moving a planar grating into the beam path and steering the zeroth diffraction order onto a microchannel plate (MCP) / phosphor screen assembly that is placed 12.5 m downstream from the HHG cell.

An XUV pulse energy of 56 nJ was measured behind 2 Al filters using an XUV photodiode (AXUV100G) placed 12.5 m downstream from the HHG cell. We estimated an XUV pulse energy of 0.7 μJ directly behind the gas cell. Considering the transmission of a new Al filter (≈ 40 %) that was used for the experiment (note that different Al filters have different transmissions, because the transmission decreases over time due to oxidization and / or deposition of material) and the reflectivity of the XUV focusing mirror (≈ 25 %), the XUV pulse energy in the VMIS experiment is expected to be ≈ 70 nJ. We have further estimated the XUV beam waist radius in the VMIS as 1.3 μm (see below). The nonlinearity of the HHG process is expected to lead to the production of XUV pulses that are substantially shorter than the duration of the driver pulse. Indeed, previous measurements have reported HHG pulse durations which are shorter than the fundamental pulse duration by factors ranging from 1.6 to 2.9 [20, 21]. Accordingly, assuming an XUV pulse duration of 4 fs, the XUV peak intensity is estimated as 7×10^{14} W/cm^2. We note that the actual XUV peak intensity might be even higher due to the attosecond pulse train structure of HHG.

To demonstrate and investigate the utility of the focused XUV pulses for XUV nonlinear optics, CDI and XUV pump - XUV probe experiments, we have studied multiphoton ionization of Ar atoms, and observed the generation of ions with charge states up to Ar^{5+}. The spatial ion distributions along the XUV propagation direction (Fig. 3) are peaked at the XUV focal plane and become narrower for more highly charged ions, which is a signature of the higher orders of nonlinearity leading to the production of these ions. We note that the absence of sidebands in the electron spectrum shown in Fig. 2(b) demonstrates that the residual NIR light did not play a role in the ionization of Ar. The spatially resolved measurements allow us to determine the relative contributions of the different ion species in the fo-

cal plane (Fig. 3(e)), showing significant contributions of Ar^{2+} (27.5 %), Ar^{3+} (19.5 %) and Ar^{4+} (3 %) ions as well as a low contribution of Ar^{5+} (0.05 %) ions. These results are comparable to previously obtained FEL results [6].

We have used the longitudinal Ar^{2+} and Ar^{3+} ion distributions (solid curves in Fig. 3(f)) to estimate the Rayleigh length z_R of the focused XUV beam. For this measurement, we have inserted a second Al filter with a transmission of 16 % to avoid saturation of the individual ion yields. The transversely integrated ion yield scales with $I^n(z) \times w^2(z) \propto I^n/I = I^{n-1}$, where $I(z) \propto 1/w^2(z)$ is the XUV intensity as a function of the distance z from the focal plane, n is the order of nonlinearity, and $w(z) = w_0\sqrt{1+z^2/z_R^2}$ is the beam radius, with w_0 being the beam waist radius. Accordingly, the ion distributions are proportional to $(1+z^2/z_R^2)^{-(n-1)}$. As indicated by measurements of the intensity dependence of the ion yields (see below), we assumed that the generation of Ar^{2+} requires the absorption of 2 photons, while the generation of Ar^{3+} requires the absorption of 4 photons. Fits using these orders of nonlinearity are shown as dotted curves in Fig. 3(f), giving $z_R = 49$ μm for the fit of the Ar^{2+} and $z_R = 58$ μm for the fit of the Ar^{3+} result. Therefore, we conclude that $z_R = 54 \pm 8$ μm. The XUV beam radius on the MCP / phosphor screen was measured to be 1.7 mm, indicating an XUV beam radius $w_{XUV,mirror} = 1.8$ mm on the XUV focusing mirror due to the divergence of the XUV beam. The beam waist radius is estimated according to $w_0 = w_{XUV,mirror} \times (1 + f_{XUV}^2/z_R^2)^{-1/2} \approx w_{XUV,mirror} \times z_R/f_{XUV}$, giving a value of 1.3 ± 0.2 μm.

Fig. 4 shows the intensity-dependent Ar^{2+}, Ar^{3+} and Ar^{4+} ion yields, from which we can extract the orders of nonlinearity of the different ion species. We find $n = 1.8 \pm 0.2$ for Ar^{2+}, $n = 3.9 \pm 0.2$ for Ar^{3+} and $n = 8.2 \pm 0.9$ for Ar^{4+}, indicating that about 8 XUV photons are absorbed in the latter case. While we have not recorded intensity-dependent data for Ar^{5+} due to the low signal, we estimate that 3-4 additional photons are required to generate Ar^{5+} from the Ar^{4+} ground state, which has an ionization potential of 74.8 eV [22]. This suggests that at least 10 HHG photons are absorbed by a single atom.

We note that the production of ions up to Ar^{4+} was observed in a recent experiment using HHG, in which XUV pulses with energies of up to 230 μJ were reported [12]. Our findings demonstrate that we achieve a higher degree of ionization, although our XUV pulse energy is more than two orders of magnitude lower than the pulse energy reported in Ref. [12]. Our results therefore open a path for the investigation of highly nonlinear processes in the XUV range using HHG sources that are driven by lasers with moderately high pulse energies, which makes it straightforward to perform these experiments using lasers at kHz repetition rates in the future.

In summary, we have demonstrated the generation of XUV pulses by HHG reaching intensities up to 7×10^{14} W/cm^2 on target using a novel scaling scheme. These XUV pulses enabled highly nonlinear ionization of Ar atoms up to Ar^{5+}, following the absorption of at least 10 XUV photons. Our results provide excellent opportunities for XUV pump - XUV probe experiments and for the single-shot CDI of isolated nanotargets.

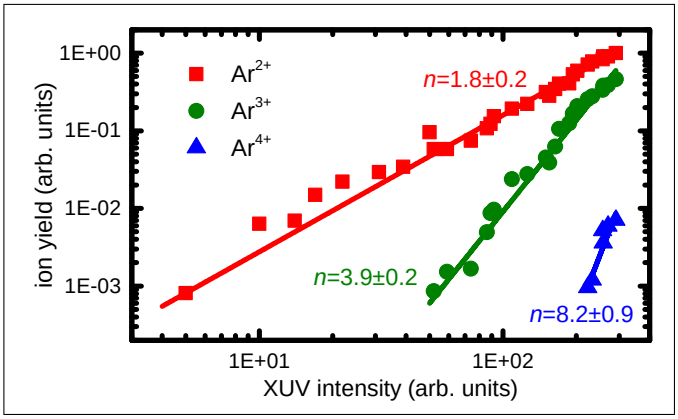

FIG. 4: Ion yields as a function of the XUV intensity (symbols) that was varied by changing the gas pressure in the HHG cell. The Ar^+ ion yield observed far away from the focus was used to calibrate the relative XUV intensities. Fits to the different ion species (solid curves) indicate orders of nonlinearities n of 1.8 ± 0.2 for Ar^{2+}, 3.9 ± 0.2 for Ar^{3+} and 8.2 ± 0.9 for Ar^{4+}. Note that the maximal XUV peak intensity in this measurement was somewhat lower compared to the measurements shown in Fig. 3.

Funding. Leibniz Grant No. SAW/2017/MBI4.

Acknowledgment. We kindly acknowledge the technical support by M. Krause, C. Reiter, W. Krüger and R. Peslin.

Disclosures. The authors declare no conflict of interest.

* daniela.rupp@ethz.ch
† bernd.schuette@mbi-berlin.de

[1] Y. H. Jiang, A. Rudenko, O. Herrwerth, L. Foucar, M. Kurka, K. U. Kühnel, M. Lezius, M. F. Kling, J. van Tilborg, A. Belkacem, K. Ueda, S. Düsterer, R. Treusch, C. D. Schröter, R. Moshammer, and J. Ullrich, Phys. Rev. Lett. **105**, 263002 (2010).
[2] P. Tzallas, E. Skantzakis, L. Nikolopoulos, G. D. Tsakiris, and D. Charalambidis, Nat. Phys. **7**, 781 (2011).
[3] E. J. Takahashi, P. Lan, O. D. Mücke, Y. Nabekawa, and K. Midorikawa, Nat. Commun. **4**, 2691 (2013).
[4] M. J. Bogan, W. H. Benner, S. Boutet, U. Rohner, M. Frank, A. Barty, M. M. Seibert, F. Maia, S. Marchesini, S. Bajt, *et al.*, Nano Lett. **8**, 310 (2008).
[5] D. Rupp, N. Monserud, B. Langbehn, M. Sauppe, J. Zim-

mermann, Y. Ovcharenko, T. Möller, F. Frassetto, L. Poletto, A. Trabattoni, *et al.*, Nat. Commun. **8**, 493 (2017).

[6] K. Motomura, H. Fukuzawa, L. Foucar, X.-J. Liu, G. Prümper, K. Ueda, N. Saito, H. Iwayama, K. Nagaya, H. Murakami, M. Yao, A. Belkacem, M. Nagasono, A. Higashiya, M. Yabashi, T. Ishikawa, H. Ohashi, and H. Kimura, J. Phys. B **42**, 221003 (2009).

[7] L. Foglia, F. Capotondi, R. Mincigrucci, D. Naumenko, E. Pedersoli, A. Simoncig, G. Kurdi, A. Calvi, M. Manfredda, L. Raimondi, *et al.*, Phys. Rev. Lett. **120**, 263901 (2018).

[8] E. Savelyev, R. Boll, C. Bomme, N. Schirmel, H. Redlin, B. Erk, S. Düsterer, E. Müller, H. Höppner, S. Toleikis, *et al.*, New J. Phys. **19**, 043009 (2017).

[9] F. Krausz and M. Ivanov, Rev. Mod. Phys. **81**, 163 (2009).

[10] B. Schütte, M. Arbeiter, T. Fennel, M. J. Vrakking, and A. Rouzée, Phys. Rev. Lett. **112**, 073003 (2014).

[11] B. Manschwetus, L. Rading, F. Campi, S. Maclot, H. Coudert-Alteirac, J. Lahl, H. Wikmark, P. Rudawski, C. Heyl, B. Farkas, *et al.*, Phys. Rev. A **93**, 061402 (2016).

[12] A. Nayak, I. Orfanos, I. Makos, M. Dumergue, S. Kühn, E. Skantzakis, B. Bodi, K. Varju, C. Kalpouzos, H. Banks, *et al.*, Phys. Rev. A **98**, 023426 (2018).

[13] B. Bergues, D. E. Rivas, M. Weidman, A. A. Muschet, W. Helml, A. Guggenmos, V. Pervak, U. Kleineberg, G. Marcus, R. Kienberger, D. Charalambidis, P. Tzallas, H. Schröder, F. Krausz, and L. Veisz, Optica **5**, 237 (2018).

[14] W. Boutu, T. Auguste, J. P. Caumes, H. Merdji, and B. Carré, Phys. Rev. A **84**, 053819 (2011).

[15] C. M. Heyl, C. L. Arnold, A. Couairon, and A. L'Huillier, J. Phys. B **50**, 013001 (2016).

[16] E. J. Takahashi, H. Hasegawa, Y. Nabekawa, and K. Midorikawa, Opt. Lett. **29**, 507 (2004).

[17] E. Gustafsson, T. Ruchon, M. Swoboda, T. Remetter, E. Pourtal, R. López-Martens, P. Balcou, and A. L'Huillier, Opt. Lett. **32**, 1353 (2007).

[18] M. Kretschmar *et al.*, in preparation.

[19] A. T. J. B. Eppink and D. H. Parker, Rev. Sci. Instrum. **68**, 3477 (1997).

[20] J. Mauritsson, P. Johnsson, R. López-Martens, K. Varju, W. Kornelis, J. Biegert, U. Keller, M. Gaarde, K. Schafer, and A. L'Huillier, Phys. Rev. A **70**, 021801 (2004).

[21] Y. Nabekawa, H. Hasegawa, E. J. Takahashi, and K. Midorikawa, Phys. Rev. Lett. **94**, 043001 (2005).

[22] E. BiÉmont, Y. Frémat, and P. Quinet, At. Data and Nucl. Data Tables **71**, 117 (1999).